International Journal of Robotics and Control Systems
Vol. 6, No. 1, 2026, pp. 651-669
ISSN 2775-2658
http://pubs2.ascee.org/index.php/ijrcs

RBFPI_STASMRC Control Strategy for SPIM Drives in Electric Vehicle Applications

Ngoc Thuy Pham [a,1,*]

[a] Faculty of Electrical Engineering Technology, Industrial University of Ho Chi Minh City
[1] Ngocpham1020@gmail.com
* Corresponding Author

ARTICLE INFO

Article history
Received November 15, 2025
Revised January 26, 2025
Accepted February 26, 2026

Keywords
RBF Tuning PID Control;
Super-Twisting Sliding Mode;
Six Phase Induction Motor;
FOC Vector Control;
RBF Neural Networks

ABSTRACT

Electric vehicle (EV) drive systems demand control strategies with fast torque response, strong disturbance rejection, and reliable real-time operation; however, conventional schemes often degrade under dynamic operating conditions. To address these limitations, this paper applies an intelligent adaptive hybrid control structure to the field-oriented control (FOC) of a six-phase induction motor (SPIM) for EV traction drive applications. The main research contribution of this work is twofold. First, an adaptive RBF neural-network-tuned PI controller in the outer speed loop is integrated with a Super-Twisting Sliding Mode controller augmented by a plug-in Repetitive Controller (STSM-RC) in the inner current loop, enabling mitigation of inter-loop coupling effects, harmonic current components, and robustness degradation under uncertainties. Second, the proposed hybrid control architecture is systematically applied and evaluated in an EV-oriented context, providing performance insights under dynamic loading and real-time execution constraints not explicitly addressed in prior SPIM control studies. The STSM-RC current controller ensures finite-time convergence, robust current regulation, and effective suppression of chattering and periodic disturbances, enabling smooth torque production. Meanwhile, the adaptive RBF-PI speed controller identifies SPIM nonlinear dynamics online and automatically adjusts control gains to maintain accurate speed tracking under varying load conditions. Comparative results demonstrate improved dynamic response, enhanced robustness, and reduced steady-state errors compared with conventional control schemes. The effectiveness of the proposed approach is validated through MATLAB/Simulink simulations and real-time simulations executed on a CPU-based OPAL-RT OP5707 platform, with system responses monitored using an external oscilloscope.

1. Introduction

In recent years, six-phase induction motor (SPIM) drive systems have gained increasing attention due to their high torque capability, improved efficiency, reduced torque ripple, enhanced fault tolerance, and lower voltage and current stress per inverter leg [1], [2]. These advantages make SPIM drives well suited for demanding applications such as railway traction, electric ship propulsion, aerospace, and, in particular, electric vehicle (EV) traction systems, where high reliability and fast torque response under dynamic operating conditions are critical. EV propulsion drives are required to operate efficiently over a wide speed range while maintaining rapid torque response during acceleration, regenerative braking, and load disturbances. In this context, SPIM drives provide compelling benefits for EV applications, including inherent fault tolerance, reduced current stress, and improved thermal performance, which directly enhance system reliability and operational safety.

However, EV-oriented operating conditions-such as frequent speed transients, load torque fluctuations, and harmonic disturbances induced by power electronic converters-pose significant challenges to conventional PI-based FOC schemes. Fixed-gain controllers often suffer from degraded tracking accuracy and limited robustness when subjected to such highly dynamic scenarios. Therefore, the development of advanced control strategies that can simultaneously ensure fast dynamic response, strong disturbance rejection, and real-time feasibility is of critical importance for SPIM-based EV traction drives [3], [4].

Numerous nonlinear control approaches have been explored to mitigate these issues, including linear output-feedback methods [5], [6], sliding-mode control (SMC) [6]-[10], backstepping techniques [11]-[15], fuzzy-logic-based controllers [16]-[19], and neural-network-based schemes [20]-[25]. Although these methods can improve robustness, they often demand high computational resources, rely on precise system modeling, and may exhibit limited performance when applied individually to highly nonlinear systems. These limitations have motivated the development of hybrid control strategies for SPIM drives [26]-[59]. Specifically, hybrid neural-network-based control methods help to enhance nonlinear control capability by approximating complex motor dynamics. While such approaches can improve tracking performance under uncertainties, they often suffer from high computational complexity, sensitivity to learning parameters, and convergence issues. Moreover, many neural-network-based controllers do not provide explicit Lyapunov-based stability proofs, which restricts their applicability in real-time and safety-critical EV traction systems. First-order sliding mode control (SMC) offers strong robustness and fast current regulation in SPIM drives; however, its discontinuous control action induces chattering, leading to increased switching losses and degraded current and torque quality. In addition, first-order SMC alone is generally insufficient to effectively suppress harmonic and periodic disturbances inherent in inverter-fed SPIM systems. Conventional PI controllers with fuzzy-logic-based gain tuning are widely used in SPIM drive systems due to their simple structure and intuitive design. Although fuzzy-tuned PI controllers can improve robustness against parameter variations and load disturbances, their performance largely depends on heuristic rule bases and membership functions, resulting in limited adaptability under highly dynamic operating conditions and a lack of rigorous stability guarantees in multiphase drive applications.

To overcome the limitations of fixed-gain PI controllers in high-performance SPIM drives, this work adopts an RBF-based PI structure in the outer speed loop. The RBF neural network continuously captures the nonlinear characteristics of the machine and adjusts the PI gains online, allowing the speed controller to maintain good dynamic response, enhanced robustness, and low steady-state error across different operating conditions while preserving the simplicity required in industrial systems. For the inner current loops, where fast dynamics and strong disturbance rejection are essential, a hybrid controller combining the Super-Twisting Sliding Mode (STSM) algorithm with an improved second-order sliding-mode structure is employed. This design mitigates the chattering and excessive control effort commonly associated with conventional SMC while ensuring finite-time convergence and high accuracy. To further suppress periodic and harmonic disturbances typically present in inverter-fed SPIM drives, a plug-in repetitive controller (RC) is integrated into the STSM framework. This combination significantly enhances current-tracking precision and improves the rejection of load-torque harmonics within the FOC scheme. The effectiveness of the proposed approach is validated through MATLAB/Simulink simulations and real-time simulations executed on a CPU-based OPAL-RT OP5707 platform, with system responses monitored using an external oscilloscope. The paper is organized into five sections, in Section 2, the basic theory of the model of the SPIM and the SPIM drive are presented. Section 3 introduces the proposed RBF NN tuning PI _STSM controller. Simulation and discuss are presented in Section 4. Finally, the concluding is provided in Section 5.

2. Model of SPIM Drives and Vehicle Propulsion

The proposed drive system consists of a six-phase induction motor supplied by a six-leg voltage-source inverter (SPVSI) through a common DC-link, as depicted in Fig. 1. To facilitate the analysis

and controller design, the Vector Space Decomposition (VSD) method is employed. Instead of working directly in the original six-dimensional stator variable space, the VSD approach reformulates the machine quantities into three orthogonal two-dimensional subspaces: the fundamental subspace responsible for torque and flux production, and two auxiliary subspaces which do not contribute to the electromagnetic energy conversion.

This decomposition is performed using a 6×6 linear transformation matrix, which maps the phase variables into the corresponding orthogonal components in the stationary reference frame. The detailed form of the matrix and its derivation can be found in standard VSD-based modeling literature [1]. By separating the controllable (energy-converting) and uncontrollable, the VSD technique significantly simplifies the control structure of the SPIM drive and allows independent design of the fundamental and harmonic-mitigation controllers.

$$T_6 = \frac{1}{3}\begin{bmatrix} 1 & \frac{\sqrt{3}}{2} & -\frac{1}{2} & \frac{\sqrt{3}}{2} & -\frac{1}{2} & 0 \\ 0 & \frac{1}{2} & \frac{\sqrt{3}}{2} & \frac{1}{2} & \frac{\sqrt{3}}{2} & -1 \\ 1 & \frac{\sqrt{3}}{2} & \frac{1}{2} & \frac{\sqrt{3}}{2} & \frac{1}{2} & 0 \\ 0 & \frac{1}{2} & \frac{\sqrt{3}}{2} & \frac{1}{2} & \frac{\sqrt{3}}{2} & -1 \\ 1 & 0 & 1 & 0 & 1 & 0 \\ 0 & 1 & 0 & 1 & 0 & 1 \end{bmatrix} \quad (1)$$

To develop the dynamic model of the six-phase induction motor, several standard simplifying assumptions are adopted. The stator and rotor windings are considered to be sinusoidally distributed, magnetic saturation is neglected, and both core losses and mutual leakage effects are ignored. Under these assumptions, the electrical and mechanical behavior of the SPIM can be expressed in the stationary reference frame, leading to the following mathematical representation of the stator and rotor voltage-current relationships.

$$\begin{aligned} [V_s] &= [R_s][I_s] + P([L_s][I_s] + [L_m][I_r]) \\ 0 &= [R_r][I_r] + P([L_r][I_r] + [L_m][I_s]) \end{aligned} \quad (2)$$

where: [V], [I], [R], [L] and [Lm] are voltage, current, resistant, self and mutual inductance vectors, respectively. P is differential operator. Subscript r and s related to the rotor and stator resistance respectively. Since the rotor is squirrel cage, [Vr] is equal to zero. The electromechanical energy conversion only takes place in the DQ subsystem. The torque equation can be written as follows:

$$T_e = 3n_p(\Psi_{rQ} i_{rd} - \Psi_{\mathrm{rD}} i_{rQ} \quad (3)$$

where: respectively, Te, np, ΨrD, ΨrQ, irD, irQ are the electromagnetic torque that generated by the motor, number of pairs of poles, the rotor flux, rotor current, respectively.

Direct control of the SPIM in the stationary reference frame is generally difficult, as the stator and rotor currents appear as time-varying sinusoidal quantities, similar to the case of conventional three-phase induction machines. To simplify the control design and obtain current components with DC characteristics, the machine model is commonly transformed into the rotating (dq) reference frame. This requires applying a suitable coordinate transformation that maps the stationary (D,Q) variables into the synchronously rotating (d,q) coordinates. The corresponding transformation matrix used to perform this mapping is expressed as follows:

$$T_{dq} = \begin{bmatrix} \cos(\delta_r) & -\sin(\delta_r) \\ \sin(\delta_r) & \cos(\delta_r) \end{bmatrix} \quad (4)$$

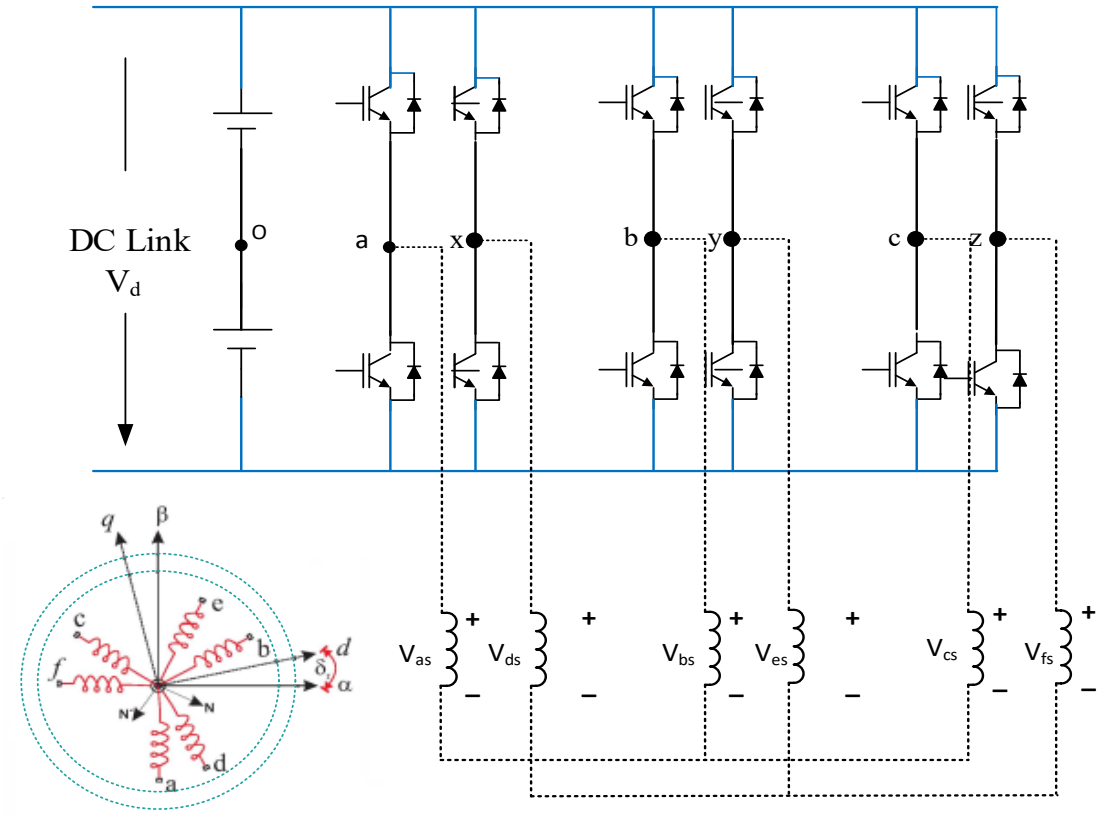

Fig. 1. A SPIM drive general diagram

where δr is the rotor angular position referred to the stator as shown in Fig. 1.

Under the field-oriented control (FOC) framework, the motor variables are transformed into the synchronous (dq) reference frame, where the flux- and torque-producing components become decoupled and appear as DC quantities in steady state. Using the coordinate transformation together with the relationships in (1) and (4), the six-phase induction motor model can be rewritten in compact space-vector form. The resulting differential equations describe the stator flux, rotor flux, and electromagnetic torque dynamics directly in the (dq) rotating frame, providing a convenient basis for controller design.

$$\begin{cases} \dfrac{d\omega}{dt} = \dfrac{3}{2} n_p \dfrac{S\sigma L_s}{J}\left(\Psi_{rd} i_{sQ}\right) - \dfrac{T_L}{J} - B\omega \\ d\Psi_{rd} = \dfrac{L_m}{\tau} i_{sD} - \dfrac{1}{\tau_r}\Psi_{\mathrm{rd}} \\ L_s \dfrac{di_{sD}}{dt} = -a i_{sD} + L_s \omega_s i_{sD} + b_r R_r \Psi_{rd} + c u_{sD} \\ L_s \dfrac{di_{sQ}}{dt} = -a i_{sQ} + L_s \omega_s i_{sD} + b_r \omega_r \Psi_{rd} + c u_{sQ} \end{cases} \tag{5}$$

Where

$$\sigma = 1 - \frac{L_m^2}{L_s L_r}; \delta = \frac{L_m}{\sigma L_s L_r}; \alpha = \frac{L_m^2 R_r + L_r^2 R_s}{\sigma L_r^2}; c = \frac{1}{\sigma}; b = \frac{L_m^2 R_r}{\sigma L_r^2}$$

The electromagnetic torque and the sliding frequency are expressed as follows:

$$T_e = \frac{3}{2} n_p \frac{L_m}{L_r} \Psi_{\mathrm{r}} i_{sQ} \tag{6}$$

$$\omega_{sl} = \frac{L_m}{L_r}\Psi_r i_{sQ} \tag{7}$$

To propel the EV, the SPIM must generate torque for the wheels as performing in Fig. 2, This illustrate the proposed transmission diagram in electric vehicle. Key factors influencing the EV's dynamic model include road conditions, inclines, acceleration ability, aerodynamic resistance, etc. The proposed control strategy takes these dynamics into account. The model is based on vehicle mechanics and aerodynamics principles [18]. The total tractive force is given by:

$$F_{te} = F_{rr} + F_{hc} + F_{ad} + F_{la} + F_{wa} \tag{8}$$

Accordingly, Eq. (8) can be rewritten as Eq. (9).

$$F_{te} = \mu_{rr} mg + mg \sin f + \frac{1}{2}\rho A C_d v^2 + m\frac{dv}{dt} + F_L \tag{9}$$

where Fte: tractive force; Frr: rolling resistance; Fhc: hill climbing force; Fla: linear acceleration force; Fwa: angular acceleration force; m: EV mass; g: gravitational acceleration; v: vehicle speed; μrr: rolling resistance coefficient; ρ: air density; A: frontal area; Cd: drag coefficient; f: slope angle; FL: external disturbance; r: wheel radius; G: gear ratio; T: required torque; vr: motor speed. In Fig. 3, under FOC, the electromagnetic torque Te is expressed simply as:

$$T_m = \frac{rF_{te}}{G} \tag{10}$$

$$P = vF_{te} = v(\mu_{rr} mg + mg \sin f + \frac{1}{2}\rho A C_d v^2 + m\frac{dv}{dt} + F_L) \tag{11}$$

Under the FOC strategy, the electromagnetic torque can be simplified as:

$$T_e = K_t i_{sq} \tag{12}$$

where Kt is the torque constant; isq is the stator current component in the dq frame.

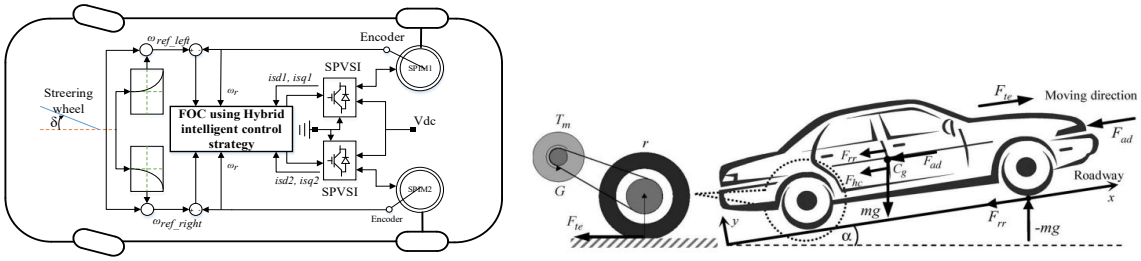

Fig. 2. Proposed transmission diagram in EV (left) and Mechanical forces acting on EV (right) [18]

The power required to drive the EV at speed v must compensate for the resistive forces:

From the vehicle dynamic model (1)-(3), the required torque of the in-wheel motor can be expressed as:

$$\frac{T_m}{n} = T_{motor} = K_t i_{sq} \tag{13}$$

where isq is the stator current command corresponding to the desired torque; n is the number of traction motors in the EV. The torque equation for the in-wheel SPIM is given by:

$$T_e = J\frac{d\omega_r}{dt} + B\omega_r + T_{motor} \tag{14}$$

$$T_e = J\frac{d\omega_r}{dt} + B\omega_r + \frac{T_m}{n} \quad (15)$$

where J is the moment of inertia of the in-wheel SPIM including the tire; B is the viscous coefficient. Assuming constant SPIM parameters, the overall EV dynamic model including the SPIM torque equation is written as:

$$T_e = \left(J + m\frac{r^2}{nG^2}\right)\frac{d\omega_r}{dt} + B\omega_r + \frac{r}{nG}\left(\mu_{rr}mg + \frac{1}{2}\rho AC_d v^2 + mg\sin\phi + F_L\right) \quad (16)$$

Simplifying gives:

$$T_e = \left(J + m\frac{r^2}{nG^2}\right)\frac{d\omega_r}{dt} + B\omega_r + T_L \quad (17)$$

Where TL is the load torque including effects from rolling resistance, aerodynamic drag, road slope, and external disturbances.

3. The Proposed Hybrid Control Structure for SPIM Drives

3.1. RBF_PI Control for Outer Speed Control

3.1.1. RBF Control

The Radial Basis Function (RBF) neural network used in the speed loop is a three-layer feedforward structure with a single hidden layer. Although the output layer is linear, the network exhibits nonlinear mapping characteristics through the radial basis functions. RBF networks possess universal approximation capability and can represent nonlinear dynamics with high accuracy. In addition, their training process is simple and free from local-minimum issues, allowing fast convergence and making them suitable for real-time adaptation in SPIM speed control.

Suppose the input vector of the RBF is x= [x1, x2, … xn]T ; the radial vector is h= [h1, h2, … hn]T; where hj is Gaussian function with the following mathematical relation:

$$h_j = exp\left[-\frac{\|X - C_j\|^2}{2b_j^2}\right](j = 1,2,\dots,m) \quad (18)$$

The center vector of the network at node j, the radial width vector and weight vector W of the network: cj= [cj1, cj2, …. cjm,]T. The radial basis width vector B and are: b= [b1, b2, …. bm,]T where bj is the basis width parameter of node, and is greater than zero; The weight vector of the network is w and w= [w1, w2, …. jm,]T . Network output is.

$$y_m(k) - w_1h_1 + w_2h_2 + \cdots + w_mh_m \quad (19)$$

Defining a performance index function is.

$$E(k) = \frac{1}{2}[y(k) - y_m(k)]^2 \quad (20)$$

According to the gradient descent method, the iterative algorithm of weight output, node center and radial basis width parameters can be written as:

$$w_j(k) = w_j(k-1) + \Delta w + \alpha[w_j(k-1) - w_j(k-2)] \quad (21)$$

$$b_j(k) = b_j(k-1) + \eta\Delta b_j + \alpha[b_j(k-1) - b_j(k-2)] \quad (22)$$

$$c_{ji}(k) = c_{ji}(k-1) + \eta\Delta b_{ji} + \alpha[c_{ji}(k-1) - c_{ji}(k-2)] \quad (23)$$

$$\Delta w_j(k) = -\eta[y(k) - y_m(k)]h_j \tag{24}$$

$$\Delta b_j = [y(k) - y_m(k)]w_j h_j \frac{\|X - C_j\|^2}{b_j^3} \tag{25}$$

$$\Delta c_{ji}(k) = [y_{out}(k) - y_m(k)]w_j \frac{x_j - c_{ji}}{b_j^2} \tag{26}$$

where η is learning rate, α is momentum factor. The Jacobian algorithm is:

$$\frac{\partial_y(k)}{\partial \Delta u(k)} \approx \frac{\partial y_m(k)}{\partial \Delta u(k)} = \sum_{j=1}^{m} w_j h_j \frac{c_{ji} - x_1}{b_j^2} \tag{27}$$

3.1.2. RBF_PI Controller

In the incremental PI scheme, the control action is computed from the variation of the tracking error rather than its absolute magnitude. The error at each sampling instant is defined simply as:

$$\varepsilon(k) = y^*(k) - y_m(k) = \omega_r^*(k) - \omega_r(k) \tag{28}$$

The controller inputs consist of the speed tracking error and its related variation signals, defined as:

$$\begin{aligned} xc(1) &= \varepsilon(k) - \varepsilon(k-1) \\ xc(2) &= \varepsilon(k) \end{aligned} \tag{29}$$

Based on these inputs, the incremental PI controller updates its output using the change in error:

$$\Delta u(k) = k_p[xc(1)] + k_1[xc(2)] \tag{30}$$

The NN updates the PI indicators online by adjusting its weights according to the current error signals:

$$E(k) = \frac{1}{2}\varepsilon^2(k) \tag{31}$$

The PI gains are updated online using gradient-based adaptation:

$$\begin{cases} \Delta k_p = -\eta \dfrac{\partial E}{\partial k_p} = -\eta \dfrac{\partial E}{\partial y}\dfrac{\partial y}{\partial \Delta u}\dfrac{\partial \Delta u}{\partial k_p} = \eta\varepsilon(k)\dfrac{\partial y}{\partial \Delta u}xc(1) \\ \Delta k_1 = -\eta \dfrac{\partial E}{\partial k_I} = -\eta \dfrac{\partial E}{\partial y}\dfrac{\partial y}{\partial \Delta u}\dfrac{\partial \Delta u}{\partial k_I} = \eta\varepsilon(k)\dfrac{\partial y}{\partial \Delta u}xc(2) \end{cases} \tag{32}$$

where ∂y/∂Δu is the Jacobian information in Eq. (27), the nonlinear behavior is captured online by the RBF NN, which provides the updated parameters for the PI controller. The configuration of the RBF-based PI controller is illustrated in Fig. 3.

3.2. STSM for the Inner Current Control Loops

The enhanced nonlinear sliding surfaces for the current control loops are defined based on the (d)- and (q)-axis current errors as follows [60], [61]:

$$S_m(k) = \begin{bmatrix} S_1(k) \\ S_2(k) \end{bmatrix} = \begin{bmatrix} \varepsilon_{isd} + \lambda_1 . |\varepsilon_{isd}|^{1/2} sat(\varepsilon_{isd}) \\ \varepsilon_{isq} + \lambda_2 . |\varepsilon_{isq}|^{1/2} sat(\varepsilon_{isq}) \end{bmatrix} \tag{33}$$

where: $\lambda_{1,2}$ are positive coefficients. The stator current errors are defined as the differences between the reference and measured current components:

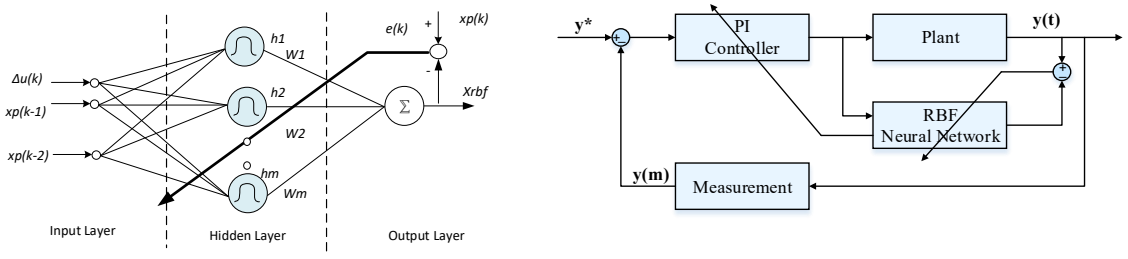

(a) (b)

Fig. 3. The structure of the RBF NN (a) and The RBF-PI control structure (b)

$$\begin{cases} \varepsilon_{isd} = i_{sd}^{*} - i_{sd} \\ \varepsilon_{isq} = i_{sq}^{*} - i_{sq} \end{cases} \tag{34}$$

We assume that the disturbance vector (d_m(k)) exhibits periodic behavior with a fundamental period (N) [35]:

$$d_m(k) = \begin{bmatrix} d_1(k) \\ d_2(k) \end{bmatrix} = \begin{bmatrix} d_1(k-N) \\ d_2(k-N) \end{bmatrix} = d_m(k-N) \tag{35}$$

Based on the disturbance-rejection condition in [35], the sliding function vector is defined as:

$$S_m(k+1) = \phi S_m(k) + \begin{bmatrix} \mu_1 sat(s_1(k)) \\ \mu_2 sat(s_2(k)) \end{bmatrix} + \quad \gamma[d_m(k) - d_m(k-N)] \tag{36}$$

where: ϕ,$\mu_{1,2}$ are positive coefficients. The control expression:

$$[u(k)] = [u_m(k) + u_m^{dis}(k)] \tag{37}$$

Based on the super-twisting algorithm [35], $[u_m(k)]$ are defined:

$$[u_m(k)] = \begin{bmatrix} u_1(k) \\ u_2(k) \end{bmatrix} = \begin{bmatrix} c_1|s_1(k)|^{1/2} sat(s_1(k)) + b_1 \int sat(s_1(k))dt \\ c_2|s_2(k)|^{1/2} sat(s_2(k)) + b_2 \int sat(s_2(k))dt \end{bmatrix} \tag{38}$$

where: $c_{1,2}$,$b_{1,24}$: are positive coefficients. $\left[u_m^{dis}(k)\right]$ are the disturbance vectors be given the system to cancel periodic disturbances and they are defined:

$$\left[u_m^{dis}(k)\right] = \begin{bmatrix} u_1^{dis}(k) \\ u_2^{dis}(k) \end{bmatrix} = \begin{bmatrix} \varepsilon_{isd}(k) + \gamma_1 sat(s_1(k+1)) \\ \varepsilon_{isq}(k) + \gamma_2 sat(s_2(k+1)) \end{bmatrix} \tag{39}$$

where: $\gamma_{1,2,}$ are positive coefficients. Lyapunov functions are chosen:

$$V = \frac{1}{2}[V_1^2 + V_2^2] = \frac{1}{2}[s_1(k)^2 + s_2(k)^2] \tag{40}$$

Differentiate both sides Eq. (40) we get:

$$\frac{dV}{dt} = \left[s_1(k)\frac{ds_1(k)}{dt} + s_2(k)\frac{ds_2(k)}{dt}\right]$$

$$\text{where:} \begin{cases} \frac{ds_1(k)}{dt} = \frac{d[\varepsilon_{isd} + \lambda_1.|\varepsilon_{isd}|^{1/2} sat(\varepsilon_{isd})]}{dt} \\ \frac{ds_2(k)}{dt} = \frac{d\left[\varepsilon_{isq} + \lambda_2.|\varepsilon_{isq}|^{1/2} sat(\varepsilon_{isq})\right]}{dt} \end{cases} \Rightarrow \begin{cases} \frac{ds_1(k)}{dt} = \frac{d[i_{sd}^{*} - i_{sd}]}{dt} + \frac{d[\lambda_1.|\varepsilon_{isd}|^{1/2} sat(\varepsilon_{isd})]}{dt} \\ \frac{ds_2(k)}{dt} = \frac{d[i_{sq}^{*} - i_{sq}]}{dt} + \frac{d\left[\lambda_2.|\varepsilon_{isq}|^{1/2} sat(\varepsilon_{isq})\right]}{dt} \end{cases} \tag{41}$$

On the other hand, to satisfy the stability condition according to Lyapunov theory, the sliding surface differential function is chosen as follows:

$$\frac{ds_m(k)}{dt} = -\left[u_m(k) + u_m^{dis}(k)\right] \tag{42}$$

Combining expressions Eq. (5); Eq. (33) - Eq. (41), u^*_{sd}, u^*_{sq} virtual control vectors are chosen as follows:

$$\begin{cases} u_{sd}^*(k) = \frac{L_s}{c}\left\{\frac{di_{sd}^*}{dt} + ai_{sd} - L_s\omega_e i_{sq} - b\psi_{rd} + \frac{d[\lambda_1.|\varepsilon_{isd}|^{1/2}sat(\varepsilon_{isd})]}{dt} + \left[u_1(k) + u_1^{dis}(k)\right]\right\} \\ u_{sq}^*(k) = \frac{L_s}{c}\left\{\frac{di_{sq}^*}{dt} + ai_{sq} - L_s\omega_e i_{sd} - b_r\omega_e\psi_{rd} + \frac{d\left[\lambda_2.|\varepsilon_{isq}|^{1/2}sat(\varepsilon_{isq})\right]}{dt} + \left[u_2(k) + u_2^{dis}(k)\right]\right\} \end{cases} \tag{43}$$

3.3. Stability Analysis

The Lyapunov function for the closed-loop system is given in Eq. (40). Taking its time derivative yields (41). By combining expressions Eq. (41) and Eq. (42), we obtain:

$$\frac{dV}{dt} = -\left[s_1(k)\left[u_1(k) + u_1^{dis}(k)\right] + s_2(k)\left[u_2(k) + u_2^{dis}(k)\right]\right]$$

$$\text{With: } \begin{cases} [s_1(k)] = \left[\varepsilon_{\psi rd} + \lambda_1.|\varepsilon_{\psi rd}|^{1/2}sat(\varepsilon_{\psi rd})\right] \\ [u_1(k)] = [c_1|s_1(k)|^{1/2}sat(s_1(k)) + b_1\int sat(s_1(k))dt] \\ \left[u_1^{dis}(k)\right] = \varepsilon_{\psi rd}(k) + \gamma_1 sat(s_1(k+1)) \end{cases} \Rightarrow \; s_1(k)\left[u_1(k) + u_1^{dis}(k)\right] > 0\forall\varepsilon_{\psi rd} \tag{44}$$

$$\begin{cases} [s_2(k)] = [\varepsilon_{\omega r} + \lambda_3.|\varepsilon_{\omega r}|^{1/2}sat(\varepsilon_{\omega r})] \\ [u_2(k)] = \left[c_2|s_2(k)|^{1/2}sat(s_2(k)) + b_2\int sat(s_2(k))dt\right] \\ \left[u_2^{dis}(k)\right] = \varepsilon_{\omega r}(k) + \gamma_3 sat(s_3(k+1)) \end{cases} \Rightarrow \; s_2(k)\left[u_2(k) + u_2^{dis}(k)\right] > 0\forall\varepsilon_{\omega r}$$

From equation (44) we get:

$$\frac{dV}{dt} < 0 with \forall\{\lambda;\gamma;\mu > 0\} \tag{45}$$

Thus, the system is always stable according to Lyapunov stability theory.

4. Simulation and Real-Time Verification Using the OPAL-RT OP5707XG System

The vector-controlled IFOC induction motor drive system is investigated through both numerical simulation and real-time verification to comprehensively evaluate the performance of the proposed control strategy. The overall control structure is implemented in MATLAB/Simulink, as illustrated in Fig. 4, where the proposed RBFPI STASMRC controller is compared with the conventional PI and RBFPI SM based schemes under identical operating conditions. In addition, real-time validation is carried out using a CPU-based OPAL-RT OP5707XG platform to assess real-time feasibility and implementation effectiveness. The combined simulation and real-time studies provide a systematic validation framework for the proposed control approach. SPIM parameters: 220V, 50 Hz, 4 pole, 1450 rpm. Rs = 10.1Ω, Rr = 9.8546Ω, Ls = 0.833457 H, Lr = 0.830811 H, Lm = 0.783106H, Ji = 0.0088 kg.m2.

4.1. Simulation Model and Test Conditions

4.1.1. The Performance of the Proposed Controllers Under Speed-Reversal Responses and Rated Load

To quantitatively evaluate the dynamic performance, the PI, RBFPI-SM, and proposed RBFPI-STASMRC controllers are tested under identical Simulink conditions, including the same motor parameters, sampling time, reference speed profile, and rated load torque. A speed-reversal

test from 130 rad/s to −130 rad/s is applied at t = 2.5 s. The rated load torque is applied at t = 1.5 s and removed at t = 3s to emphasize transient behavior and disturbance rejection capability.

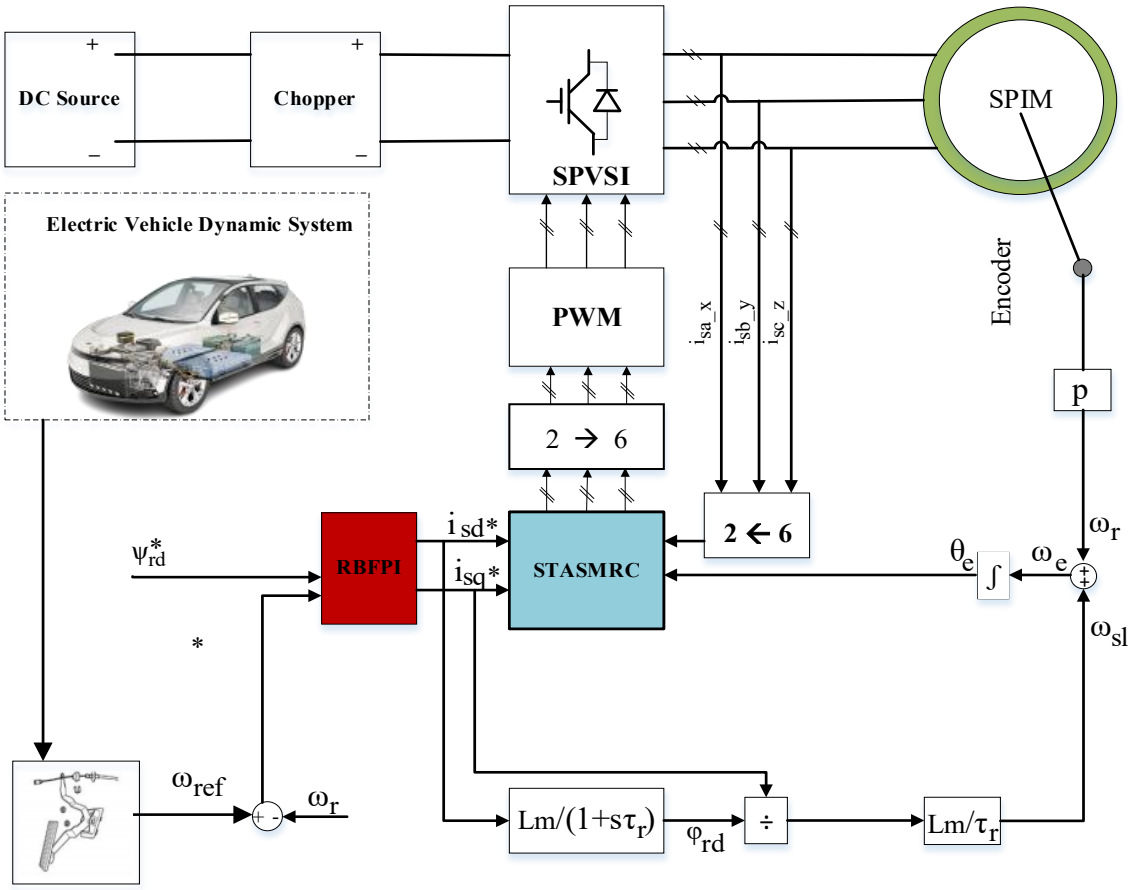

Fig. 4. SPIM drive system employing the proposed control architecture for EV applications

As shown in Fig. 5 and summarized in Table X, the conventional PI controller exhibits the longest settling time and the highest overshoot, reflecting its limited robustness under nonlinear and load-varying conditions. The RBFPI-SM scheme improves transient performance by reducing overshoot and error indices; however, residual tracking errors remain. In contrast, the proposed RBFPI-STASMRC controller achieves the shortest settling time and significantly lower ISE and IAE values, confirming superior dynamic response and faster error convergence.

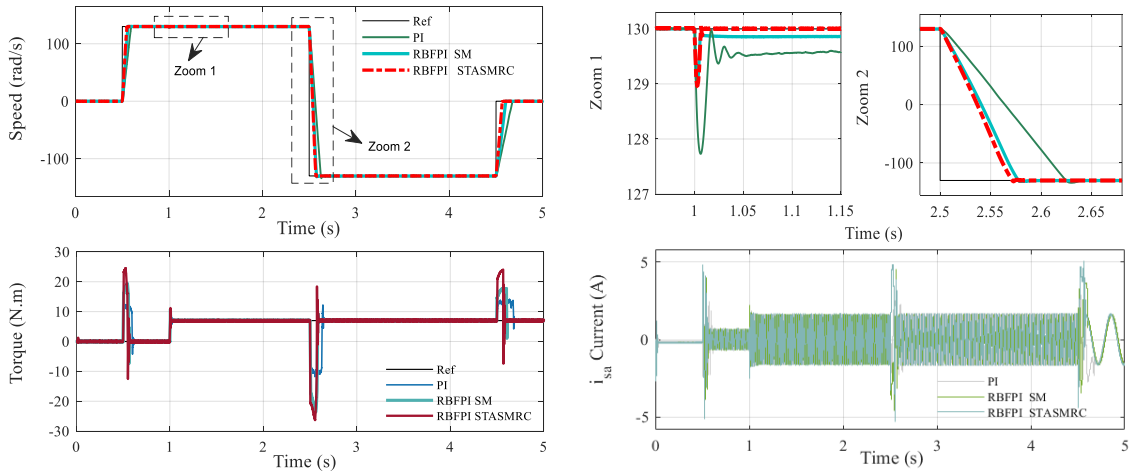

Fig. 5. Simulink- The dynamic performance of PI, RBFPI-SM, and proposed RBFPI-STASMRC control schemes, showing the speed, torque, and i_{sa} stator current

4.1.2. The Performance of the Proposed Controllers Under Disturbance Load

Fig. 6 presents the robustness evaluation of the PI, RBFPI-SM, and proposed RBFPI-STASMRC controllers under rated load disturbance conditions. The responses include rotor speed, electromagnetic torque, and phase-a stator current, with a zoomed view highlighting transient behavior. The conventional PI controller exhibits noticeable speed deviation and slow recovery when the load disturbance is applied. The RBFPI-SM approach improves disturbance rejection by reducing the speed dip; however, residual oscillations remain during transient intervals. In contrast, the proposed RBFPI-STASMRC controller maintains the speed response close to the reference with minimal deviation and faster recovery. Moreover, the RBFPI-STASMRC scheme produces smoother torque dynamics and reduced current oscillations compared with PI and RBFPI-SM controllers, confirming superior robustness and enhanced current regulation under load variations.

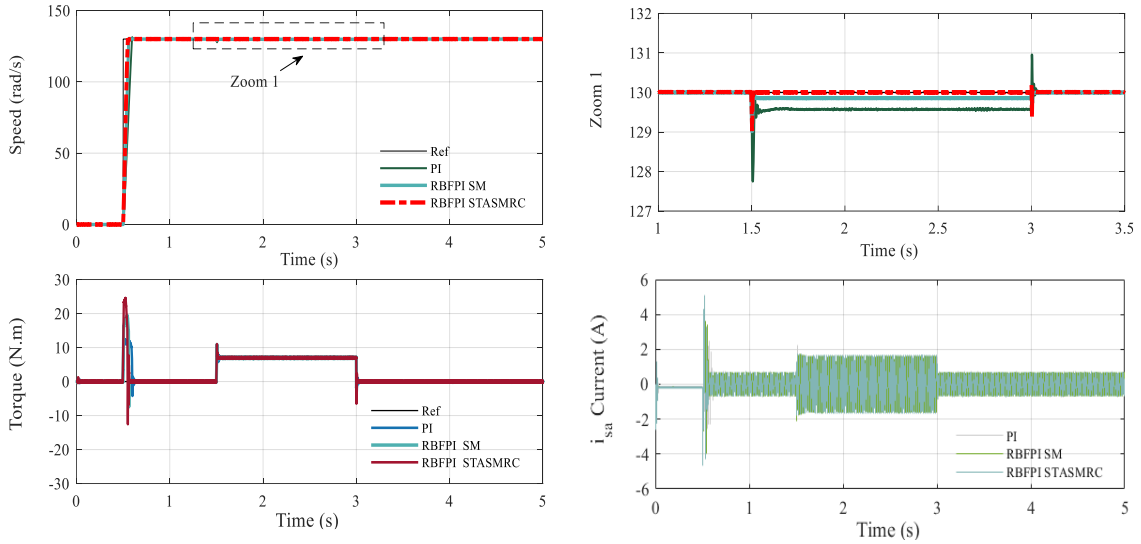

Fig. 6. Simulink the robustness of PI, RBFPI SM and RBFPI STASMRC under load disturbance showing the speed, torque, and i_{sa} current

4.1.3. Speed-Tracking Performance of the Proposed RBFPI STASMRC Under EV Driving Cycles

To further evaluate the applicability of the proposed control strategy under realistic EV operating conditions, its speed-tracking performance is investigated using representative electric vehicle driving cycles, specifically improved ECE-15 and ECE-25. Fig. 7 presents the speed-tracking performance of the proposed RBFPI-STASMRC-controlled SPIM drive under the Improved ECE-15 and Improved ECE-25 driving cycles. The results demonstrate that the proposed control strategy accurately follows rapidly varying speed references with negligible steady-state error and smooth transient behavior throughout acceleration and deceleration phases. Despite frequent speed changes and highly dynamic operating conditions, the controller maintains stable tracking without noticeable oscillations or delay. These results confirm the capability of the proposed RBFPI-STASMRC scheme to meet realistic EV traction requirements, ensuring fast dynamic response and robust operation under time-varying speed commands.

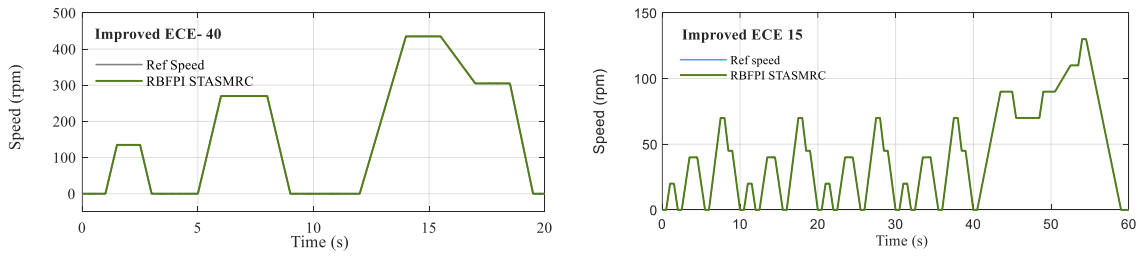

(a) (b)

Fig. 7. Simulink speed response of RBFPI STASMRC control strategy for test of ECE-15 (a) and ECE-25 (b)

4.2. Real-Time Implementation on the OPAL-RT OP5707XG

To further examine the practical applicability and real-time implementability of the proposed control strategy, the complete controller-plant system is implemented on the OPAL-RT OP5707XG real-time simulation platform. In contrast to conventional offline simulations, the adopted configuration allows simultaneous execution of the controller and the induction motor drive model under strict real-time constraints, thereby ensuring deterministic timing behavior and faithful emulation of the drive system dynamics. Under this real-time setup, the system execution is structured into coordinated software-based tasks running on the OP5707XG CPU target. Specifically, the hybrid speed and current control algorithms are executed in soft real-time mode on the CPU. The control loop operates with a sampling period of Ts=5x10e-6s (50 µs), which provides sufficient temporal resolution for rapid error compensation and high-bandwidth motor-drive operation. In addition, the two-level SVPWM inverter, the induction motor model, and the load torque disturbance module are also implemented on the same CPU target and executed in real time. This integrated configuration preserves deterministic execution while accurately capturing both electrical and mechanical system dynamics without reliance on offline computation.

For real-time observation and signal acquisition, an I/O interface is configured accordingly. The real-time I/O mapping enables analog output channels (±16 V range) from the FPGA to be directly connected to an external oscilloscope, allowing real-time visualization of key drive variables, including rotor speed, electromagnetic torque, and stator current responses. This measurement setup provides high-resolution monitoring of transient phenomena and facilitates experimental assessment of the controller performance under realistic real-time operating conditions. Based on the established real-time framework, two verification scenarios are carried out on the OP5707XG platform, comprising dynamic performance evaluation under variable-speed operation, robustness assessment against harmonic disturbances. Overall real-time execution framework on the OPAL-RT OP5707XG platform is shown in Fig. 8.

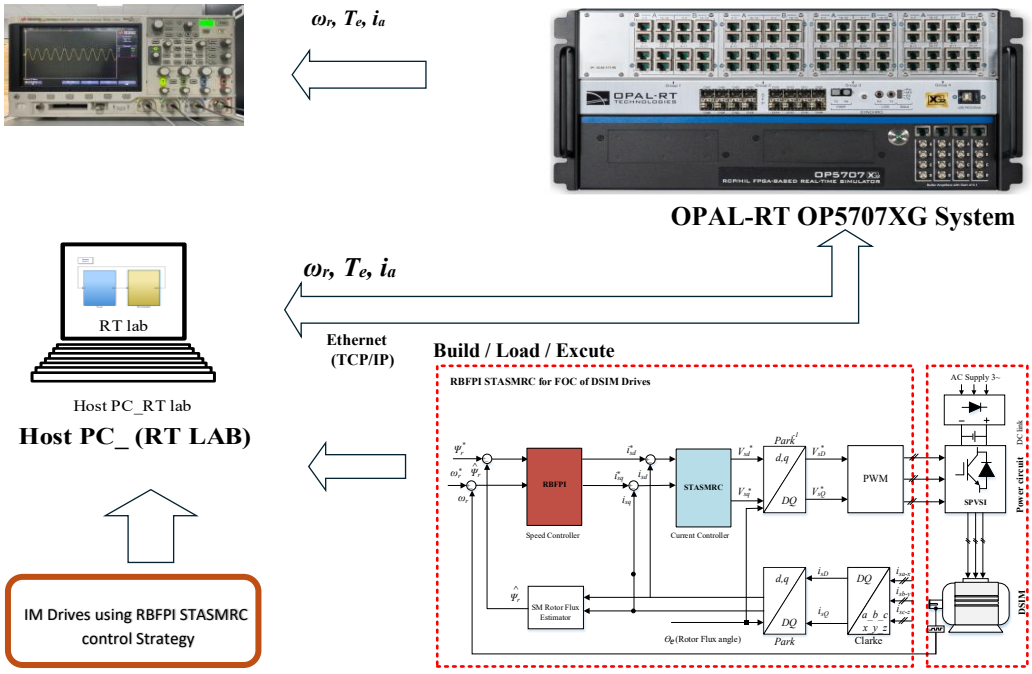

Fig. 8. Overall real-time execution framework on the OPAL-RT OP5707XG platform

4.2.1. Real-Time Validation Under Speed-Reversal and Load Disturbance Conditions

To further verify the practical feasibility and robustness of the proposed control strategy, real-time hardware-in-the-loop (HIL) experiments are conducted on a CPU-based OPAL-RT OP5707 platform under the same operating scenarios considered in the Simulink studies, including speed-

reversal and load disturbance conditions. Fig. 9 and Fig. 10 illustrate the real-time speed, electromagnetic torque, and phase-a stator current responses under no-load and rated load speed-reversal tests, while Fig. 11 presents the constant-speed responses under rated load disturbance for the RBFPI-SM and proposed RBFPI-STASMRC controllers.

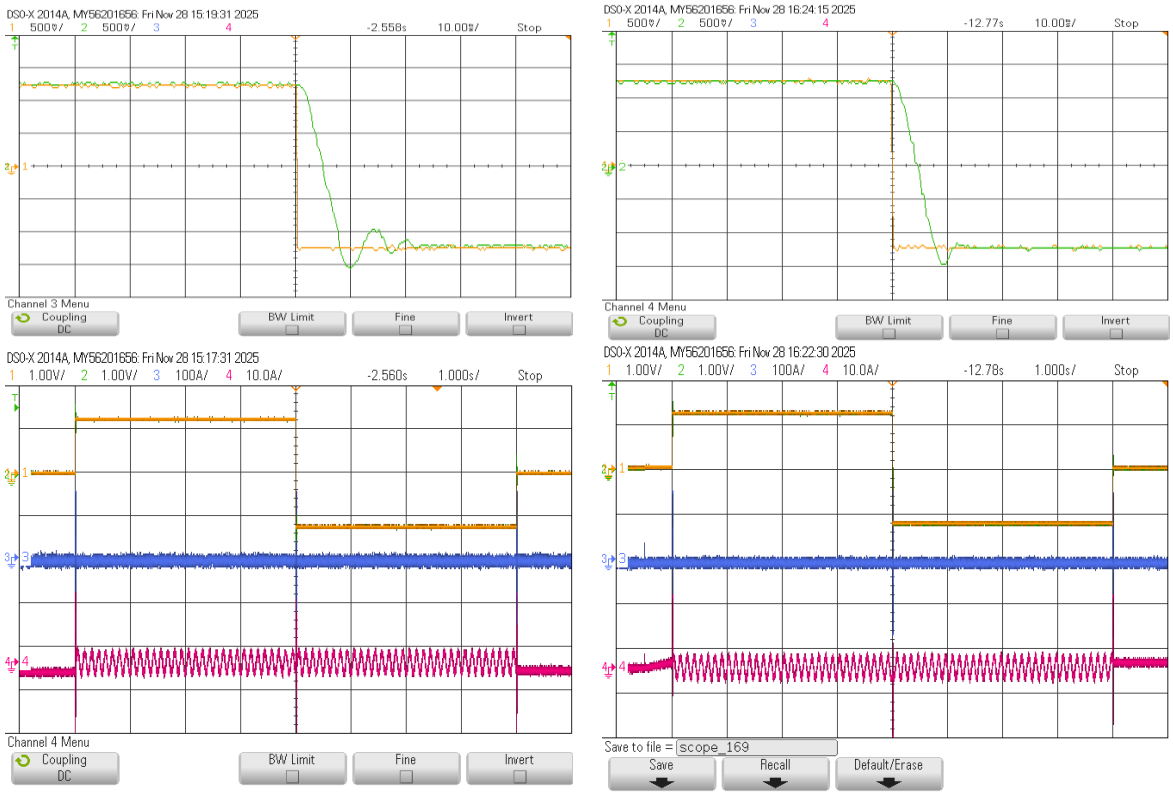

(a) (b)

Fig. 9. Real-time speed-reversal responses under no load condition for RBFPI SM (a) and RBFPI STASMRC (b), including speed, electromagnetic torque, and phase-a current

Compared with the corresponding Simulink results shown in Fig. 5 and Fig. 6, the real-time responses exhibit a high level of consistency in terms of overall dynamic behavior and relative performance trends. Under speed-reversal conditions, the proposed RBFPI-STASMRC controller achieves smoother speed transitions, reduced oscillations, and faster recovery than the RBFPI-SM scheme in both no-load and rated load cases. The torque and stator current waveforms further confirm improved robustness, with lower transient peaks and attenuated oscillations. Similarly, during load disturbance tests, the conventional RBFPI-SM controller exhibits noticeable speed deviation and pronounced oscillations in torque and current responses. In contrast, the proposed RBFPI-STASMRC controller maintains the rotor speed close to its reference with reduced deviation and faster recovery, while producing smoother torque dynamics and lower current oscillations.

Minor discrepancies between Simulink and real-time responses, especially during abrupt transients, are mainly attributed to real-time discretization effects, computational delays, and measurement noise. Nevertheless, these effects do not degrade system stability or tracking performance. Overall, the real-time results validates the effectiveness and real-time implementability of the proposed RBFPI-STASMRC control strategy for EV traction applications.

4.2.2. Real-Time Validation Speed-Tracking Performance of the Proposed RBFPI STASMRC Under EV Driving Cycles

Fig. 12 presents the real-time speed responses of the proposed RBFPI-STASMRC-controlled SPIM drive obtained based on a CPU-based OPAL-RT OP5707 platform under the ECE-15 and ECE-25 driving cycles. Compared with the corresponding Simulink results, the real-time responses exhibit a high level of consistency in terms of speed tracking accuracy and overall dynamic behavior.

Despite the presence of real-time execution constraints, sampling delays, and measurement noise, the proposed controller maintains stable operation and accurately follows the time-varying speed references without noticeable oscillations or instability. Minor deviations observed during rapid speed transitions are mainly attributed to real-time discretization and hardware latency effects and do not compromise overall tracking performance. These results confirm that the proposed RBFPI-STASMRC control strategy is suitable for real-time EV traction applications and can be effectively implemented on practical digital control platforms.

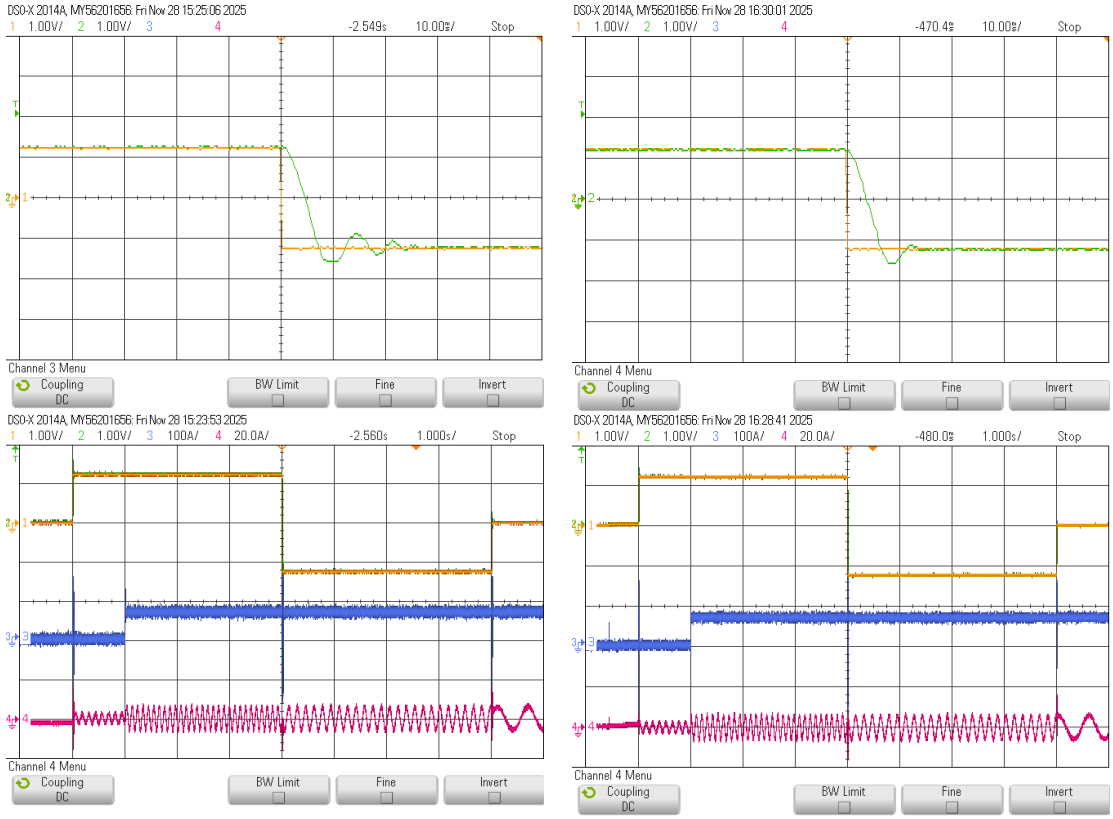

Fig. 10. Real-time speed-reversal responses under rated load condition for RBFPI SM (a) and RBFPI STASMRC (b), including speed, electromagnetic torque, and phase-a current

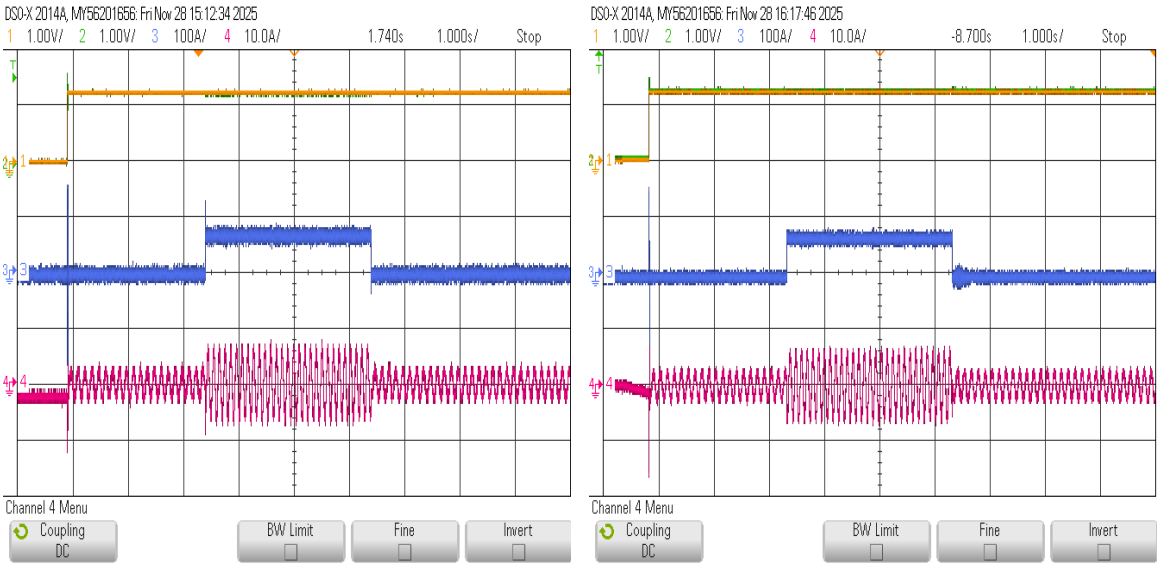

Fig. 11. Real-time constant speed responses under load disturbance for RBFPI SM (left) and RBFPI STASMRC (right): speed, electromagnetic torque, and phase-a current

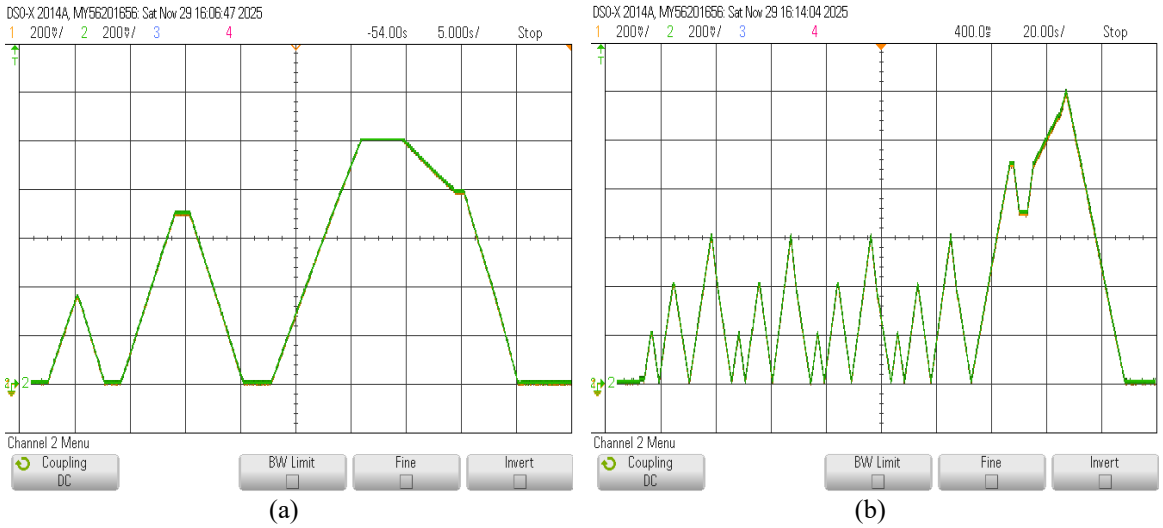

(a) (b)

Fig. 12. Real-time speed response of RBFPI STASMRC control strategy for test of ECE-15 (a) and ECE-25 (b)

5. Conclusion

This paper has presented an intelligent adaptive hybrid control structure for field-oriented control (FOC) of six-phase induction motor (SPIM) drives targeting electric vehicle (EV) traction applications. The proposed scheme integrates an RBF neural-network-tuned PI controller in the outer speed loop with a Super-Twisting Sliding Mode current controller enhanced by a plug-in Repetitive Controller (STASMRC) in the inner loops. This combination effectively exploits the learning capability of RBF-based gain tuning and the finite-time robustness of sliding-mode control to achieve improved dynamic performance and strong disturbance rejection. Comprehensive MATLAB/ Simulink simulations and real-time CPU-based validation using the OPAL-RT OP5707 platform demonstrate that the proposed control strategy provides faster transient response, reduced tracking error, smoother torque behavior, and enhanced robustness against load disturbances and parameter variations when compared with conventional PI and RBFPI-SM control schemes. The results confirm the effectiveness and real-time feasibility of the proposed hybrid control architecture for EV-oriented SPIM drive systems. Nevertheless, the present study has certain limitations. The experimental validation is currently restricted to real time CPU-based testing and does not yet include full-power hardware motor-drive experiments. In addition, while finite-time stability of the inner current loops governed by the STASMRC structure is rigorously established, the RBF neural network in the speed loop is employed as an online gain-tuning mechanism rather than a Lyapunov-synthesized adaptive controller.

Future work will therefore focus on extending the experimental validation to full hardware motor-drive platforms using DSP/FPGA-based controllers and high-power inverter systems. Moreover, further theoretical research will be devoted to developing a Lyapunov-consistent adaptive law for the RBF-based speed control loop, with the objective of establishing a unified stability framework for the complete cascaded control system, including rigorous Uniformly Ultimately Bounded (UUB) analysis of the outer speed loop. These extensions will further strengthen both the theoretical foundation and the practical applicability of the proposed control strategy for advanced EV traction drive applications.

Author Contribution: All authors contributed equally to this work. All authors read and approved the final paper.

Funding: This research received no external funding

Conflicts of Interest: The authors declare no conflict of interest.

References

[1] E. Levi, "Multiphase Electric Machines for Variable-Speed Applications," *IEEE Transactions on Industrial Electronics*, vol. 55, no. 5, pp. 1893-1909, 2008, https://doi.org/10.1109/TIE.2008.918488.

[2] J. W. Finch and D. Giaouris, "Controlled AC Electrical Drives," *IEEE Transactions on Industrial Electronics*, vol. 55, no. 2, pp. 481-491, 2008, https://doi.org/10.1109/TIE.2007.911209.

[3] H. S. Aldawsari, A. T. Ghanem, and I. M. Ismail, "Improving Power Quality under Fast Charging Structure of Electric Vehicles with STATCOM: Zebra Optimization Algorithm," *Journal of Robotics and Control (JRC)*, vol. 6, no. 6, pp. 2940-2950, 2025, https://doi.org/10.18196/jrc.v6i6.27450.

[4] M. A. Shamseldin, M. Araby, and S. El-Khatib, "A Low-Cost High Performance Electric Vehicle Design Based on Variable Structure Fuzzy PID Control," *Journal of Robotics and Control (JRC)*, vol. 5, no. 6, pp. 1713–1721, 2024, https://doi.org/10.18196/jrc.v5i6.22071.

[5] M. Kuczmann and K. Horváth, "Design of Feedback Linearization Controllers for Induction Motor Drives by using Stator Reference Frame Models," *2021 IEEE 19th International Power Electronics and Motion Control Conference (PEMC)*, pp. 766-773, 2021, https://doi.org/10.1109/PEMC48073.2021.9432503.

[6] A. Accetta *et al*., "Robust Control for High Performance Induction Motor Drives Based on Partial State-Feedback Linearization," *IEEE Transactions on Industry Applications*, vol. 55, no. 1, pp. 490-503, 2019, https://doi.org/10.1109/TIA.2018.2869112.

[7] A. Sabir and S. Ibrir, "Induction motor speed control using reduced-order model," *Automatika: časopis za automatiku, mjerenje, elektroniku, računarstvo i komunikacije*, vol. 59, no. 3–4, pp. 274–285, 2018, https://doi.org/10.1080/00051144.2018.1531963.

[8] A. Nurettin and N. İnanç, "High-Performance Induction Motor Speed Control Using a Robust Hybrid Controller With a Supertwisting Sliding Mode Load Disturbance Observer," *IEEE Transactions on Industrial Electronics*, vol. 70, no. 8, pp. 7743-7752, 2023, https://doi.org/10.1109/TIE.2022.3222625.

[9] N. T. Pham and T. D. Le, "Novel FOC Vector Control Structure Using RBF Tuning PI and SM for SPIM Drives," *International Journal of Intelligent Engineering & Systems*, vol. 13, no. 5, pp. 265-275, 2020, https://doi.org/10.22266/ijies2020.1031.38.

[10] M. Hu, H. Ahn and K. You, "Speed Tracking of SPMSM via Super-Twisting Logarithmic Fast Terminal Sliding-Mode Control," *IEEE Access*, vol. 11, pp. 91904-91912, 2023, https://doi.org/10.1109/ACCESS.2023.3308156.

[11] Y. Su, Z. Yang, X. Sun, and Q. Ding, "Backstepping control of a bearingless induction motor based on a linear extended state observer," *Electrical Engineering*, vol. 105, no. 6, pp. 4569-4579, 2023, https://doi.org/10.1007/s00202-023-01958-5.

[12] H. Chaabane, K. D. Eddine, and C. Salim, "Sensorless backstepping control using a Luenberger observer for double-star induction motor," *Archives of Electrical Engineering*, vol. 69, no. 1, pp. 241–254, 2020, https://doi.org/10.24425/aee.2020.131761.

[13] C. Chen and H. Yu, "Backstepping sliding mode control of induction motor based on disturbance observer," *IET Electric Power Applications*, vol. 14, no. 12, pp. 2537–2546, 2020, https://doi.org/10.1049/iet-epa.2020.0485.

[14] O. Mahmoudi and A. Boucheta, "Adaptive backstepping control of linear induction motors using artificial neural network for load estimation," *Indonesian Journal of Electrical Engineering and Computer Science*, vol. 26, no. 1, pp. 202–210, 2022, https://doi.org/10.11591/ijeecs.v26.i1.pp202-210.

[15] N. T. Pham, "Sensorless speed control of SPIM using BS_PCH novel control structure and NNSM_SC MRAS speed observer," *Journal of Intelligent & Fuzzy Systems*, vol. 39, no. 3, pp. 2657–2677, 2020, https://doi.org/10.3233/JIFS-190540.

[16] K. Zeb, Z. Ali, K. Saleem, W. Uddin, M. A. Javed, and N. Christofides, "Indirect field-oriented control of induction motor drive based on adaptive fuzzy logic controller," *Electrical Engineering*, vol. 99, no. 3, pp. 803–815, 2017, https://doi.org/10.1007/s00202-016-0447-5.

[17] K. H. Chao and C. L. Chang, "Design of a Robust Controller for Induction Motor Drive Systems Based on Extendable Fuzzy Theory," *Mathematics*, vol. 12, no. 20, p. 3235, 2024, https://doi.org/10.3390/math12203235.

[18] A. Haddoun, M. E. H. Benbouzid, D. Diallo, R. Abdessemed, J. Ghouili and K. Srairi, "Modeling, Analysis, and Neural Network Control of an EV Electrical Differential," *IEEE Transactions on Industrial Electronics*, vol. 55, no. 6, pp. 2286-2294, 2008, https://doi.org/10.1109/TIE.2008.918392.

[19] C. B. Regaya, F. Farhani, A. Zaafouri, and A. Chaari, "A novel adaptive control method for induction motor based on Backstepping approach using dSpace DS 1104 control board," *Mechanical Systems and Signal Processing*, vol. 100, pp. 466–481, 2018, https://doi.org/10.1016/j.ymssp.2017.07.017.

[20] W. Feng, J. Bai, and J. Zhang, "Full-order adaptive observer for interior permanent-magnet synchronous motor based on novel fast super-twisting algorithm," *Measurement and Control*, vol. 56, no. 1–2, pp. 93–113, 2023, https://doi.org/10.1177/00202940221122235.

[21] R. S. Kumar *et al.*, "A combined HT and ANN based early broken bar fault diagnosis approach for IFOC fed induction motor drive," *Alexandria Engineering Journal*, vol. 66, pp. 15–30, 2023, https://doi.org/10.1016/j.aej.2022.12.010.

[22] A. Dawood, B. M. Hasaneen, and A. M. Abdel-Aziz, "Design of an efficient neural network model for detection and classification of phase loss faults for three-phase induction motor," *Neural Computing and Applications*, vol. 36, no. 11, pp. 5827–5845, 2024, https://doi.org/10.1007/s00521-023-09387-y.

[23] H. Jie, G. Zheng, J. Zou, X. Xin and L. Guo, "Adaptive Decoupling Control Using Radial Basis Function Neural Network for Permanent Magnet Synchronous Motor Considering Uncertain and Time-Varying Parameters," *IEEE Access*, vol. 8, pp. 112323-112332, 2020, https://doi.org/10.1109/ACCESS.2020.2993648.

[24] H. Yu and T. Chen, "Valid RBFNN Adaptive Control for Nonlinear Systems With Unmatched Uncertainties," *IEEE Transactions on Neural Networks and Learning Systems*, vol. 35, no. 11, pp. 16139-16152, 2024, https://doi.org/10.1109/TNNLS.2023.3292115.

[25] H. Maghfiroh *et al*., "Induction Motor Speed Control Using PID Tuned by Particle Swarm Optimization Under Vector Control," *Buletin Ilmiah Sarjana Teknik Elektro*, vol. 7, no. 2, pp. 172-180, 2025, https://doi.org/10.12928/biste.v7i2.13112.

[26] M. N. Uddin, Z. R. Huang and A. B. M. S. Hossain, "Development and Implementation of a Simplified Self-Tuned Neuro–Fuzzy-Based IM Drive," *IEEE Transactions on Industry Applications*, vol. 50, no. 1, pp. 51-59, 2014, https://doi.org/10.1109/TIA.2013.2269131.

[27] Q. Su, W. Quan, G. Cai, and J. Li, "Improved adaptive backstepping sliding mode control for generator steam valves of non-linear power systems," *IET Control Theory & Applications*, vol. 11, no. 9, pp. 1414-1419, 2017, https://doi.org/10.1049/iet-cta.2016.1241.

[28] W. Chen, S. S. Ge, J. Wu and M. Gong, "Globally Stable Adaptive Backstepping Neural Network Control for Uncertain Strict-Feedback Systems With Tracking Accuracy Known a Priori," *IEEE Transactions on Neural Networks and Learning Systems*, vol. 26, no. 9, pp. 1842-1854, 2015, https://doi.org/10.1109/TNNLS.2014.2357451.

[29] J. Yu, B. Chen, H. Yu, C. Lin, L. Zhao, "Neural networks-based command filtering control of nonlinear systems with uncertain disturbance," *Information Sciences*, vol. 426, pp. 50-60, 2017, https://doi.org/10.1016/j.ins.2017.10.027.

[30] Z. Kang, X. Lin, Z. Liu, X. Shen, Y. Gao and J. Liu, "Adaptive Generalized Super-Twisting Sliding Mode Control for PMSM Drives," *IEEE Transactions on Energy Conversion*, vol. 41, no. 1, pp. 148-159, 2026, https://doi.org/10.1109/TEC.2025.3590203.

[31] R. Seeber and M. Reichhartinger, "Conditioned super-twisting algorithm for systems with saturated control action," *Automatica*, vol. 116, p. 108921, 2020, https://doi.org/10.1016/j.automatica.2020.108921.

[32] H. Zhang, P. Ran, and Z. Zhang, "PMSM sensorless control based on super-twisting algorithm sliding mode observer with the IAORLS parameter estimations," *Scientific Reports*, vol. 15, no. 1, p. 22386, 2025, https://doi.org/10.1038/s41598-025-04030-3.

[33] J. Liu, J. Zhu, K. Khayati, D. Zhong, and J. Jiang, "Exponential super-twisting control for nonlinear systems with unknown polynomial perturbations," *Scientific Reports*, vol. 14, no. 1, p. 3457, 2024, https://doi.org/10.1038/s41598-024-53761-2.

[34] L. Tan, J. Gao, Y. Luo, and L. Zhang, “Super-twisting sliding mode control with defined boundary layer for chattering reduction of permanent magnet linear synchronous motor,” *Journal of Mechanical Science and Technology*, vol. 35, no. 5, pp. 1829-1840, 2021, https://doi.org/10.1007/s12206-021-0403-9.

[35] A. Karami-Mollaee and O. Barambones, “Higher order sliding mode control of MIMO induction motors: A new adaptive approach,” *Mathematics*, vol. 11, no. 21, p. 4558, 2023, https://doi.org/10.3390/math11214558.

[36] J. A. Moreno, H. Ríos, L. Ovalle and L. Fridman, "Multivariable Super-Twisting Algorithm for Systems With Uncertain Input Matrix and Perturbations," *IEEE Transactions on Automatic Control*, vol. 67, no. 12, pp. 6716-6722, 2022, https://doi.org/10.1109/TAC.2021.3130880.

[37] S. Ding, Q. Hou and H. Wang, "Disturbance-Observer-Based Second-Order Sliding Mode Controller for Speed Control of PMSM Drives," *IEEE Transactions on Energy Conversion*, vol. 38, no. 1, pp. 100-110, 2023, https://doi.org/10.1109/TEC.2022.3188630.

[38] X. Lin, B. Zhang, S. Fang, R. Xu, S. Guo, and J. Liu, “Adaptive generalized super twisting sliding mode control for PMSMs with filtered high-gain observer,” *ISA Transactions*, vol. 138, pp. 639–649, 2023, https://doi.org/10.1016/j.isatra.2023.02.008.

[39] H. Li, L. Wang, H. Du and A. Boulkroune, "Adaptive Fuzzy Backstepping Tracking Control for Strict-Feedback Systems With Input Delay," *IEEE Transactions on Fuzzy Systems*, vol. 25, no. 3, pp. 642-652, 2017, https://doi.org/10.1109/TFUZZ.2016.2567457.

[40] J. Yu, P. Shi, W. Dong and H. Yu, "Observer and Command-Filter-Based Adaptive Fuzzy Output Feedback Control of Uncertain Nonlinear Systems," *IEEE Transactions on Industrial Electronics*, vol. 62, no. 9, pp. 5962-5970, 2015, https://doi.org/10.1109/TIE.2015.2418317.

[41] T. G. Workineh, Y. B. Jember, and A. T. Kassie, “Evaluation of intelligent PPI controller for the performance enhancement of speed control of induction motor,” *Scientific African*, vol. 22, p. e01982, 2023, https://doi.org/10.1016/j.sciaf.2023.e01982.

[42] S. N. Al-Bargothi, G. M. Qaryouti, and Q. M. Jaber, “Speed control of DC motor using conventional and adaptive PID controllers,” *Indonesian Journal of Electrical Engineering and Computer Science*, vol. 16, no. 3, pp. 1221–1228, 2019, https://doi.org/10.11591/ijeecs.v16.i3.pp1221-1228.

[43] M. Zhang, W. Li and M. Liu, "Adaptive PID Control Strategy Based on RBF Neural Network Identification," *2005 International Conference on Neural Networks and Brain*, pp. 1854-1857, 2005, https://doi.org/10.1109/ICNNB.2005.1614987.

[44] H. Fadil and M. L. Elhafyani, “Fuzzy-PI controller applied to PMSM speed controller: design and experimental evaluation,” *International Journal of Power Electronics*, vol. 11, no. 1, pp. 102–115, 2020, https://doi.org/10.1504/IJPELEC.2020.103952.

[45] J. K. Jain, S. Ghosh, and S. Maity, “Concurrent PI controller design for indirect vector controlled induction motor,” *Asian Journal of Control*, vol. 22, no. 1, pp. 130–142, 2020, https://doi.org/10.1002/asjc.1911.

[46] N. Goel, S. Chacko, and R. N. Patel, “PI controller tuning based on stochastic optimization technique for performance enhancement of DTC induction motor drives,” *Journal of The Institution of Engineers (India): Series B*, vol. 101, no. 6, pp. 699–706, 2020, https://doi.org/10.1007/s40031-020-00496-z.

[47] W. Yu, K. Zhu and Y. Yu, "Variable Universe Fuzzy PID Control for Active Suspension System With Combination of Chaotic Particle Swarm Optimization and Road Recognition," *IEEE Access*, vol. 12, pp. 29113-29125, 2024, https://doi.org/10.1109/ACCESS.2024.3368762.

[48] N. T. Pham, “An improved BS_NAHOSM hybrid control strategy for FOC of dual Star induction motor drives,” *Periodica Polytechnica Electrical Engineering and Computer Science*, vol. 69, no. 3, pp. 226-235, 2025, https://doi.org/10.3311/PPee.37384.

[49] Y. Xu, B. Zhang, Y. Deng, Y. Kang, X. Liu and H. Cao, "Robust Speed Control Strategy of PMSMs Using Improved Sliding-Mode Controller With New Reaching Law and Variable-Parameter Generalized Super-Twisting Observer," *IEEE Transactions on Power Electronics*, vol. 40, no. 11, pp. 16548-16559, 2025, https://doi.org/10.1109/TPEL.2025.3592251.

[50] H. Li, B. Song, T. Chen, Y. Xie, and X. Zhou, "Adaptive fuzzy PI controller for permanent magnet synchronous motor drive based on predictive functional control," *Journal of the Franklin Institute*, vol. 358, no. 15, pp. 7333–7364, 2021, https://doi.org/10.1016/j.jfranklin.2021.07.024.

[51] A. Abougarair, M. Aburakhis, M. Bakouri, and A. Ma'arif, "Comparative Performance Analysis of LQR Based PSO and Fuzzy Logic Control for Active Car Suspension," *Buletin Ilmiah Sarjana Teknik Elektro*, vol. 7, no. 3, pp. 270–295, 2025, https://doi.org/10.12928/biste.v7i3.13237.

[52] W. Bu, S. Guo, Z. Fan, and J. Li, "Improved adaptive PI-like fuzzy control strategy of permanent magnet synchronous motor," *Energies*, vol. 18, no. 2, p. 362, 2025, https://doi.org/10.3390/en18020362.

[53] X. D. Liu, K. Li, and C. H. Zhang, "Improved backstepping control with nonlinear disturbance observer for the speed control of permanent magnet synchronous motor," *Journal of Electrical Engineering & Technology*, vol. 14, no. 1, pp. 275–285, 2019, https://doi.org/10.1007/s42835-018-00021-9.

[54] M. Ghibeche, K. Kouzi, A. Ouanouki, D. Difi, B. Nail, I. E. Tibermacine, and A. Ma'arif, "Advanced Predictive DTC for Double-Star PMSM Using PI-Regulated Switching," *International Journal of Robotics and Control Systems*, vol. 6, no. 1, pp. 190-203, 2025, https://doi.org/10.1049/esi2.12117.

[55] B. Mohapatra, B. K. Sahu, and S. Pati, "A novel optimally tuned super twisting sliding mode controller for active and reactive power control in grid-interfaced photovoltaic system," *IET Energy Systems Integration*, vol. 5, no. 4, pp. 491-511, 2023, https://doi.org/10.1049/esi2.12117.

[56] X. Xiong, H. Chen, Y. Lou, Z. Liu, S. Kamal and M. Yamamoto, "Implicit Discrete-Time Adaptive First-Order Sliding Mode Control With Predefined Convergence Time," *IEEE Transactions on Circuits and Systems II: Express Briefs*, vol. 68, no. 12, pp. 3562-3566, 2021, https://doi.org/10.1109/TCSII.2021.3070435.

[57] N. T. Pham, "Design of Novel STASOSM Controller for FOC Control of Dual Star Induction Motor Drives," *International Journal of Robotics & Control Systems*, vol. 4, no. 3, pp. 1059-1074, 2024, https://doi.org/10.31763/ijrcs.v4i3.1443.

[58] P. Proaño, R. Díaz, C. Chillán, J. Medina, W. Chamorro, and J. Zuñiga, "Sliding mode control proposed using a Clegg integrator for speed control of a three-phase induction motor," *Engineering Proceedings*, vol. 77, no. 1, p. 8, 2024, https://doi.org/10.3390/engproc2024077008.

[59] T. Wang, B. Wang, Y. Yu and D. Xu, "Discrete Sliding-Mode-Based MRAS for Speed-Sensorless Induction Motor Drives in the High-Speed Range," *IEEE Transactions on Power Electronics*, vol. 38, no. 5, pp. 5777-5790, 2023, https://doi.org/10.1109/TPEL.2023.3236024.

[60] Y. Shtessel, C. Edwards, L. Fridman, and A. Levant, "Sliding Mode Control and Observation," *Springer*, vol. 10, pp. 978-970, 2014, https://doi.org/10.1007/978-0-8176-4893-0.

[61] N. Derbel, J. Ghommam, Q. Zhu, "Applications of Sliding Mode Control," *Springer*, 2017, https://doi.org/10.1007/978-981-10-2374-3.